Role of $E\times B$ drift in divertor detachment control via boron powder injection on EAST

Lei Peng[a], Zhen Sun[b], Jizhong Sun[a,*], Rajesh Maingi[b], Guozhang Jia[c], Xavier Bonnin[d], Fang Gao[e], GuiZhong Zuo[c,*], Wei Xu[c], Weikang Wang[a], Jinyuan Liu[a]

[a] *Key Laboratory of Materials Modification by Laser, Ion, and Electron Beams (Ministry of Education), Dalian University of Technology, Dalian 116024, People's Republic of China*

[b] *Princeton Plasma Physics Laboratory, Princeton, NJ 08543, United States of America*

[c] *Institute of Plasma Physics, Chinese Academy of Sciences, Hefei 230031, China*

[d] *ITER Organization, Route de Vinon-sur-Verdon, CS 90 046, 13067 St-Paul-lez-Durance, France*

[e] *School of Computer and Communication Engineering, Dalian Jiaotong University, Dalian 116028, People's Republic of China*

jsun@dlut.edu.cn

Abstract

The effects of B powder injection on plasma detachment about EAST discharge were studied by using SOLPS-ITER code package with the effects of $\boldsymbol{E}\times\boldsymbol{B}$ drifts considered. The simulation results show that plasma detachment occurs at the inner target in favourable toroidal magnetic field ($\boldsymbol{B}_t$) direction at a relatively low B powder flow rate, one order of magnitude lower than that at the outer target. In a similar scenario with unfavourable $\boldsymbol{B}_t$, it is found that the detachment thresholds of B flow rate for both the inner and outer targets are close and of the same order as that for the outer target with favourable $\boldsymbol{B}_t$. In favourable $\boldsymbol{B}_t$ direction at B powder flow rate of 1.2×10^{21} atoms/s, a localized, broadened high-density region is formed near the inner target benefitted by the injection location and the $\boldsymbol{E}\times\boldsymbol{B}$ drift, and a radiation-intensified zone, mostly contributed by B^{1+} and B^{2+}, occurs there. The $\boldsymbol{E}\times\boldsymbol{B}$ drift facilitates plasma detachment at the inner target and simultaneously amplifies the in-out divertor asymmetry. In addition, the simulation results with three different injection locations show that the injection from outer strike point leads to the lowest Z_{eff} inside the separatrix and has an intermediate flow rate for detachment at the outer target, comparing with the X-point and upstream locations.

Keywords: B powder injection, $\boldsymbol{E}\times\boldsymbol{B}$ drift, plasma detachment, radiation, SOLPS-ITER

1. Introduction

The control of excessive particle and heat flux deposited on the divertor target plates is a key issue for the long-pulse and high-parameter operation of tokamak devices [1–3]. For ITER, the unmitigated steady-state heat flux will reach 40 MW/m^2, much greater than the steady-state heat flux limit of 10 MW/m^2, for the tungsten material used in ITER divertor target plates [4]. Therefore, it is imperative to achieve divertor detachment to reduce the heat flux toward the target plates and other plasma-facing walls, and avoid or mitigate damage to the plasma facing components (PFCs). Plasma detachment is considered to be an effective means for achieving long pulse operation in modern tokamaks and is a natural continuation of the high recycling conditions to higher density and stronger impurity radiation loss [5]. However, the upstream density cannot be raised at our will due to limitations imposed by the H-mode density limit [6] and Greenwald density limit [7]. In practice, plasma detachment can be achieved by enhancing the local radiation through the introduction of a certain amount of impurity into the divertor region. Experimental studies worldwide have shown that the heat flux at the target plates can be controlled effectively, and plasma detachment can even be realized by puffing impurity gases such as N_2, Ne, and Ar into the divertor region [8–10]. However, high (and even medium) Z impurities have adverse impacts on the core plasma, by contaminating it and degrading energy confinement; in the worst case, the impurities can even terminate the discharge. It was reported that nitrogen is of concern in a reactor environment due to the production of tritiated ammonia, which contaminates the uranium beds of the ITER tritium plant [11]. Therefore, it is desirable to reduce these unwanted effects on the core plasma by injecting low-Z impurities instead. Numerical studies have suggested that alternative impurities such as boron (B) deserve consideration for radiative dissipation as well [12–14]. Boron has much larger cooling efficiency in low temperature range (1-10 eV) than neon [14]. In addition, B is a popular material for real-time wall conditioning in current fusion devices and future device, e.g., ITER.

Boron powder injection experiments have been performed in several magnetic confinement fusion devices, such as ASDEX-Upgrade [15,16], DIII-D [14,17], KSTAR [18], LHD [19–22], and EAST [23,24]. Real-time B powder injection experiments were conducted in DIII-D with an upper single null (USN) and forward toroidal magnetic field ($\boldsymbol{B}_t$) configuration [14]. The experimental results showed that a medium rate of B injection (35 mg/s) resulted in a reduction of 20 eV in peak temperature and led to heat flux detachment. The LHD device experiments [22] showed that the electron and ion temperature, and plasma stored energy were increased, on average, 27%, 25% and 17% during B powder injection under various experimental conditions; they also showed that the amplitude of plasma fluctuations reduced by a factor of two. Real-time B powder injection experiments were carried out on the EAST device [23,24]. Experimental results showed that in an USN configuration, B powder injected from R=1.570 m effectively suppressed edge localized modes (ELMs) while simultaneously reducing the transient particle and heat flux at the targets. All these experimental results demonstrated the great potential of B powder injection for mitigating ELMs, improving wall conditions, and reducing heat flux.

In this work, we focus on the reduction of heat flux and the plasma detachment by B powder injection. Previous work [12] has shown that B powder injection has little effect on upstream parameters, and therefore, the divertor region is our concern in this paper. Among various factors such as $\boldsymbol{E}\times\boldsymbol{B}$ drift, ballooning transport, divertor geometry, magnetic field configuration, etc., the $\boldsymbol{E}\times\boldsymbol{B}$ drift is considered to be one of the important factors affecting plasma properties in the divertor region for a tokamak discharge [25–27]. EAST experiments [26] indicated that in the favourable $\boldsymbol{B}_t$ direction, the outer divertor detached at a higher core plasma density than the inner divertor; in this case, the $\boldsymbol{E}\times\boldsymbol{B}$ drifts moved particles from the outer divertor into the inner divertor. Reversing the toroidal field direction reduced the detachment threshold density in the outer divertor, and increased the threshold density in the inner divertor. The simulation results of neon seeding on EAST [27] showed that in the favourable $\boldsymbol{B}_t$, $\boldsymbol{E}\times\boldsymbol{B}$ drift could drive the Ne impurity from the outer divertor to the inner divertor through private flux region (PFR), thus promoting the achievement of detachment in inner divertor; in the unfavourable $\boldsymbol{B}_t$, the transport of Ne ions from the inner divertor to the outer divertor through the PFR was enhanced by $\boldsymbol{E}\times\boldsymbol{B}$ drift. The above results indicate that $\boldsymbol{E}\times\boldsymbol{B}$ drift significantly affects plasma detachment and particle transport. Therefore, it is very necessary to consider the effect of $\boldsymbol{E}\times\boldsymbol{B}$ drift.

To further understand the plasma detachment induced by real-time B powder injection and the influence of $\boldsymbol{E}\times\boldsymbol{B}$ drift on plasma properties in the divertor region during the injecting process, we conducted the present simulation study based on experimental data from the EAST device by using the SOLPS-ITER code. The remainder of this paper is organized as follows: section 2 briefly reviews the experimental parameters and simulation numerical setup. In section 3, we first present the experimental results in the favourable and unfavourable $\boldsymbol{B}_t$ directions, and under the similar conditions related results obtained in the simulations. Subsequently, analysis with other simulation and experimental results. Finally, section 5 presents a summary of this work.

2. Experimental and Simulation Setup

EAST (major and minor radius of 1.85 and 0.45 m, respectively) is a D-shaped cross section, fully superconducting tokamak, aiming at long-pulse high-performance H-mode plasmas. The impurity powder dropper (IPD) was implemented in the upper port of the EAST device and enables the injection of solid B powder (diameter ~70 μm) into the upper divertor region with an adjustable flow rate of ~2-250 mg/s and a gravitational velocity ~9 m/s [23,28]. The B powder injection experiments on the EAST device cover a wide range engineering and plasma parameters, such as, favorable and unfavorable $\boldsymbol{B}_\mathrm{t}$ directions, Greenwald density fraction from 0.24-0.87, pure radio frequency (RF) heating up to 5.8 MW, and with combined RF+NBI (neutral beam injection, NBI) up to 7.5 MW, and so on[23]. Real-time B powder injection discharges #85043 (in the favourable $\boldsymbol{B}_t$ direction, $\boldsymbol{B}_{Fav}$) and #93469 (in the unfavourable $\boldsymbol{B}_t$ direction, $\boldsymbol{B}_{UnF}$) with similar parameters are selected and compared in this work. The typical discharge parameters are as follows: plasma current I_p = 0.5 MA, on-axis $\boldsymbol{B}_t$ = ±2.5 T, total heating power ~ 6 MW, B powder flow rate of ~20 mg/s and USN configuration.

In the simulation, the plasma profiles are first reconstructed by SOLPS-ITER [29–31] using the experimental data as the initial input for the background plasma. The experimental data come from EAST discharge #85043 of B powder injection experiment with ion grad-B drift towards the upper X-point. The meshes used in simulations are shown in Fig. 1, including quadrilateral meshes for tracking charged particles and triangular meshes for tracing neutral particles. In the experiments, the B powder falls vertically into the plasma from R=1.57 m by gravity [28], and the corresponding injection location in the simulation grid is shown by R_1 in Fig. 1 (most of the work in the paper is carried at this injection position unless otherwise stated). The average diameter of B powder is around 70 μm [23,24], and it is assumed that it ablates completely into neutral atoms 8 cm vertically under the injection position R_1. The ablated B atoms then interact with the background plasma. The atomic physics database used for the B radiation is taken from the "year 89" ADAS database [32]. In SOLPS-ITER simulations, the impurity source is implicitly assumed to be toroidally symmetric, while in reality, it is more concentrated in the region where B powder ablates [33,34]. After being ionized, B ions move swiftly along magnetic field lines and become more or less toroidally symmetric quickly. In this work, toroidal effects are expected to be small. The injection flow rate of B powder in EAST discharges #85043 and #93469 was 20 mg/s, which corresponds to a flow rate of 1.2×10^{21} atoms/s in the simulation. Owing to the uncontrollable loss of B impurity in experiments, the B impurity flow rate entering the plasma is slightly less than the planned injection rate.

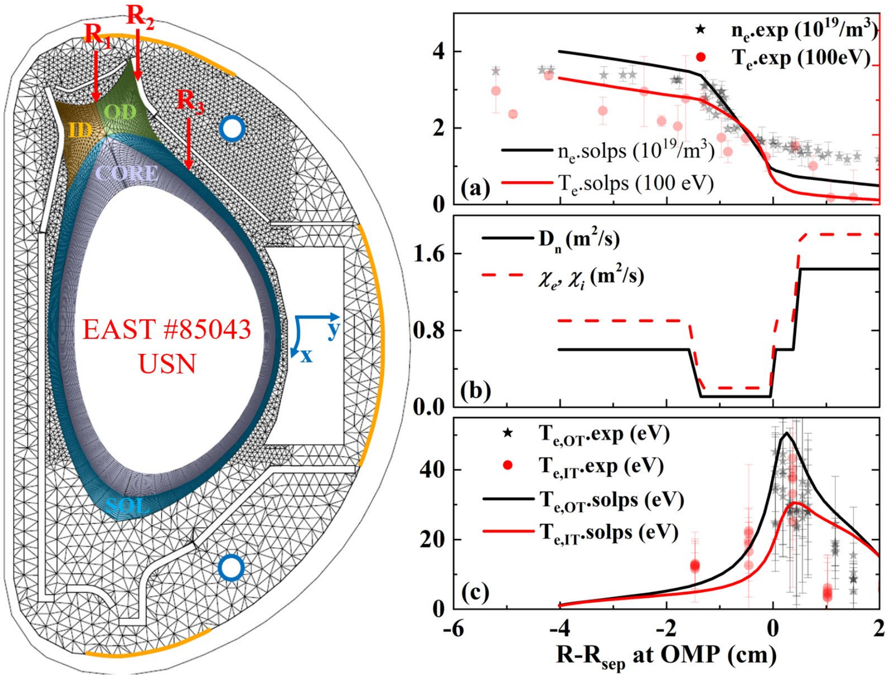

Fig. 1 Meshes (left) used in the simulation, the radial profiles of (a) upstream electron density and temperature profiles (by reflectometer and Thomson scattering, respectively; (b) radial particle and thermal diffusivity profiles at the outer mid-plane; and (c) the electron temperatures (by divertor Langmuir probes) at outer and inner targets mapped to the outer mid-plane without B injection. Each location for B powder injection is marked by a red arrow; R_1 is the experimental injection position. The quadrilateral meshes region consists of inner (ID) and outer (OD) divertors, core region (CORE) and scrape-off layer (SOL). The poloidal-coordinate (x-coordinate) varies along flux surfaces and the radial-coordinate (y-coordinate) varies perpendicular to flux surfaces.

To understand the influence of ***E***×***B*** drift on plasma detachment, we simulated the B powder injection experiment with ***E***×***B*** drift considered. The reversal of ***E***×***B*** drift direction was realized by reversing the direction of the toroidal magnetic field in the experiments and simulations. For comparison, simulations for scenarios without considering ***E***×***B*** drift contributions were also performed. Electrons, deuterium (D^0, D^+, D_2, D_2^+) and boron (B^0, B^{1+}, B^{2+}, B^{3+}, B^{4+} and B^{5+}) species are included in the simulation. Sputtering and redeposition of B ions are not considered in the present simulation. Based on experimental parameters, boundary conditions were set as follows: the deuterium ion density at the innermost boundary, $R - R_{sep} = -4.0$ cm at the outer mid-plane (OMP), was fixed at 4.0×10^{19} /m^3 and radial particle fluxes of atoms and D^+, B^{1+}, B^{2+}, and B^{3+} ions through the innermost boundary were set to zero. The radial particle flux of species B^{4+} was assumed to be -5.0×10^{17} /s ("minus" means flowing into the core region) and that of species B^{5+} was 1.0×10^{17} /s (flowing out of the core region). This boundary condition indicates that B^{4+} flowing into the core region are fully ionized to B^{5+} and then one-fifth of species B^{5+} flow back to the edge region. The inward transport of B ions was related to the convection induced by the dominant polarization effects in trapped electron mode, and the outward transport was related to the ion temperature gradient turbulence[35]. At the same time, currents contributed by viscosity, ion-neutral friction, and inertia terms were activated in cases considering ***E***×***B*** drift [36]. The power entering the computational domain from the innermost boundary was set to 3.2 MW based on experiments and was divided equally into ion and electron channels. The sheath boundary condition was applied at target plates and the leakage boundary condition was adopted for the scrape-off layer (SOL) and PFR edge [36,37]. Pumps considered in the simulation include the cryopump and the pumping port-end. The former had a recycling coefficient of 0.94, indicated by the blue line in the mesh image of Fig. 1; the latter had a recycling coefficient of 0.99 and was denoted by the orange line in the same image [36]. In the case free of B powder injection, except for the pumps, the recycling coefficients on other wall segments were set to 1.0 as all ions were assumed to return to the plasma in their neutral forms after hitting the wall. Experimentally, it has been observed that B powder injection has a much smaller effect on recycling than Li [28], and recycling coefficient with Li injection in study [38] was considered to be reduced by 20%. In this work, the recycling coefficient of D ions at the inner and outer targets was assumed to be 0.98 in cases with B powder injection.

Considering that the small effect of diamagnetic drift on divertor plasma [36,39–41], the diamagnetic drift is not taken into account in this work, and only the effect of ***E***×***B*** drift is considered. Since ***E***×***B*** drift always exists in experiments, the initial plasma profiles reconstructed numerically by SOLPS-ITER considered the $\boldsymbol{E}\times\boldsymbol{B}$ drift contribution. The initial upstream plasma profiles at the OMP reconstructed by SOLPS-ITER in the $\boldsymbol{B}_{Fav}$ configuration are shown in Fig. 1(a), and the corresponding radial particle and thermal diffusivity profiles used are shown in Fig. 1(b). The electron temperatures at the inner (IT) and outer (OT) targets mapped to OMP are also displayed in Fig. 1(c). Simulations of the discharge in the unfavourable $\boldsymbol{B}_t$ were also performed, and both discharges have similar parameters except for the toroidal magnetic field direction. Therefore, the simulations in the $\boldsymbol{B}_{UnF}$ are also based on discharge #85043, and the radial particle and thermal diffusivity coefficients in $\boldsymbol{B}_{UnF}$ were adjusted to maintain initial plasma profiles similar at the outer mid-plane in $\boldsymbol{B}_{Fav}$ and $\boldsymbol{B}_{UnF}$. To explore the influence of B powder flow rate on plasma detachment and provide a reasonable range of B flow rate for experiments, the B powder flow rate was scanned based on experimental parameters.

3. Results and discussion

3.1 Plasma detachment and in-out divertor asymmetry

Real-time B powder injection experiments showed that B powder could reduce the electron temperature effectively at targets and even achieve plasma detachment in either favourable or unfavourable $\boldsymbol{B}_t$ directions. The temporal evolutions of intensity of B_V emission, line-averaged electron density n_{eL}, upper inner (UI) and outer (UO) target electron temperature, plasma stored energy W_{MHD} and ion saturation current J_{sat} (measured by divertor Langmuir probes) in the $\boldsymbol{B}_{Fav}$ (EAST discharge #85043) and $\boldsymbol{B}_{UnF}$ (EAST discharge #93469) directions are presented in Fig. 2. Both discharge #85043 and #93469 have a similar B powder flow rate of about 20mg/s, and the nearly constant n_{eL} (Figs. 2(a) and 2(d)) indicates that the upstream plasma has little effect on the downstream. In the $\boldsymbol{B}_{Fav}$ scenario, the ion saturation current at the inner target decreases significantly and falls down to a noise level when the intensity of B_V emission reaches a threshold, and the target temperature in the vicinity of inner strike point gradually drops from ~20 eV to below 5 eV; evidently, plasma detachment is achieved at the inner target. In the counterpart of $\boldsymbol{B}_{UnF}$, electron temperature T_e near the outer strike point exhibits a significant drop from ~30 eV to ~7 eV (after ~5.2 s), and the ion saturation current at the outer targets decreases significantly after B powder injection. Note that the plasma stored energy representing the plasma performance changes slightly and is comparable for both discharges.

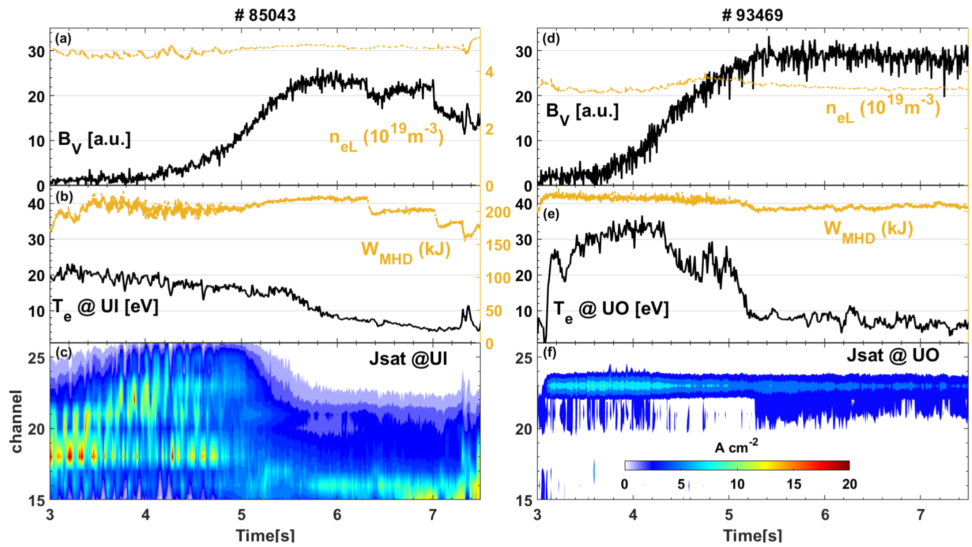

Fig. 2 The time-dependent evolution of the intensity of B_V emission, line-averaged electron density n_{eL} (yellow, right Y axis), upper inner (UI) and outer (UO) target electron temperature, plasma stored energy W_{MHD} (yellow, right Y axis), and ion saturation current J_{sat} in the favourable (#85043) and unfavourable (#93469) toroidal magnetic fields.

Experimental observations show that the heat flux to the divertor targets cannot be reduced effectively if the injection rate is too low and an excessive amount of injected impurity will contaminate the core region plasma, resulting in H-Ltransition. Figure 2 shows the target T_e and ion saturation current ramp down as the B_V ramp up from noise to a saturated level. To estimate the workable flow rate range of B powder and its threshold for plasma detachment under the discharge conditions of interest, the injection flow rate was scanned from 1.0×10^{19} to 4.9×10^{21} atoms/s in both favourable and unfavourable toroidal magnetic field directions. Figure 3 shows the separatrix density at outer mid-plane $n_{e,sep}$, peaks of electron temperature T_e, and target-perpendicular energy flux density q_t and ion flux density Γ_{ion} against B powder flow rate, respectively, for the $\boldsymbol{B}_{Fav}$ and $\boldsymbol{B}_{UnF}$. From Fig. 3(a), the impact of B powder injection on upstream separatrix density is small, with the difference between the maximal and minimal densities in the $\boldsymbol{B}_{Fav}$ and $\boldsymbol{B}_{UnF}$ being only 20% and 27%, respectively. Apart from the fact that the density undergoes a steep drop when B flow rate exceeds 4.0×10^{20} atoms/s in the $\boldsymbol{B}_{UnF}$, the density variation shows a similar trend in both toroidal magnetic directions. Corresponding to the upstream density drop in the $\boldsymbol{B}_{UnF}$, the electron temperature (Fig. 3(b)) and heat flux density (Fig. 3(c)) at the outer target also fall rapidly. The reduction in upstream density may be related to the particle flux driven by poloidal $\boldsymbol{E}_r\times\boldsymbol{B}$ drift, which is correlated with the electron temperature.

In the $\boldsymbol{B}_{Fav}$ cases, the peaks of electron temperature T_e drop monotonously at both the OT and the IT as the injection flow rate increases. When the B powder flow rate reaches 2.0×10^{20} atoms/s, the peak T_e at the IT drops below 5.0 eV, indicating that the plasma has entered into detachment state at the inner target. Meanwhile, the ion flux decreases by 28% from 8.9×10^{22} to 6.4×10^{22} $m^{-2}s^{-1}$, and the ion flux does not decrease significantly since the plasma is not in the deeply detachment. The peak T_e at the OT is 42 eV, more than eight times that at the IT, indicating that the discharge in the $\boldsymbol{B}_{Fav}$ requires a higher B powder flow rate to achieve detachment at the outer target. The scan shows that the critical flow rate for OT is as high as 4.9×10^{21} atoms/s, about four times the magnitude used in the experiment (~20 mg/s).

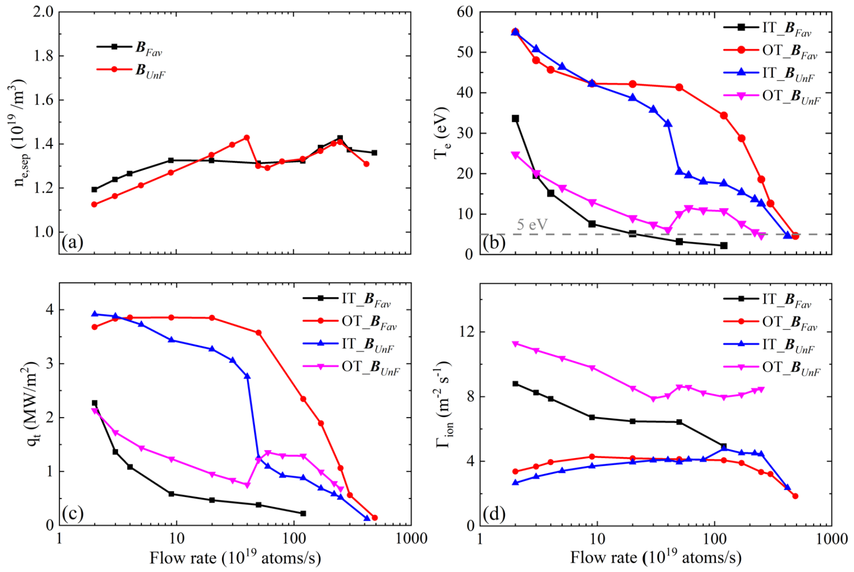

Fig. 3 Separatrix density at outer mid-plane (a); peaks of electron temperature (b) and perpendicular energy flux density (c) and ion flux density (d) at divertor targets versus the B powder flow rate in both favourable and unfavourable toroidal magnetic fields. Here, IT and OT in the legends represent inner and outer targets, respectively. Note that the horizontal coordinate is on a logarithmic scale.

As seen from Fig. 3(b), the q_t peaks towards the IT go down with increasing flow rate of B powder in the $\boldsymbol{B}_{Fav}$ cases. This result, together with the continuously decreasing particle flux at the inner target (Fig.

3(d)), indicates that the inner target plasma has started to transition towards detachment state. When plasma detachment is achieved at the IT at B powder flow rate of 2.0×10^{20} atoms/s, the q_t undergo a remarkable reduction from 2.4 to 0.5 MW/m^2 by a factor of about 5. While at the outer target, as B powder flow rate increases, q_t increases a little first (which mainly caused by the increased particle flux in Fig. 3(d)), then changes little, and at around the flow rate of 2.0×10^{20} atoms/s, q_t starts to go down.The injection of B powder gives rise to the increase in particle flux toward the targets, and the radiation induced by B powder dissipates energy. The plasma temperature then evolves according to the energy equation. When the reduction in q_t caused by radiation losses is larger than the increase in q_t induced by the change in particle flux, the q_t drops. The variation of q_t indicates that the radiation losses almost dominate the behaviour of q_t, unless the increase in particle flux plays a major role at relatively low injection flow rates. The radiation losses are analyzed in section 3.3.

In the unfavourable $\boldsymbol{B}_t$ direction, simulations with similar initial conditions as in the favourable $\boldsymbol{B}_t$ direction were carried out to look for the B powder detachment thresholds at the IT and OT. From Fig. 3(b), the peak T_e at the OT falls down to under 5 eV when the B powder flow rate is further raised to 2.5×10^{21} atoms/s, which is significantly higher than that at the IT in the $\boldsymbol{B}_{Fav}$ case. At this flow rate, the peak T_e is 13 eV at the IT, a magnitude comparable to 5.0 eV at the OT; the in-out asymmetry is not so prominent as in the $\boldsymbol{B}_{Fav}$ case. When the flow rate is raised further to 4.2×10^{21} atoms/s (which is smaller than the 4.9×10^{21} atoms/s for the OT in the $\boldsymbol{B}_{Fav}$ case), the plasma detachment is finally achieved at the IT. In Fig. 3, we also find that the electron temperature and target-perpendicular energy flux peaks do not decrease monotonically at the outer target. At the flow rate of 4.0×10^{20} atoms/s, T_e and and q_t drop to a level of almost detachment. But when the B powder flow rate exceeds 4.0×10^{20} atoms/s, they increase and a bulge forms in each of their profiles. Corresponding, the particle flux also varies, but its variation trend is slightly different from that of temperature and heat flux. This phenomenon is due to $\boldsymbol{E}\times\boldsymbol{B}$ drift and injection location, which we will discuss later.

From the simulation results presented above, the thresholds of B powder flow rate for plasma detachment are found to be very different between at the IT and OT in the two toroidal field directions. In the $\boldsymbol{B}_{Fav}$, it is easy to achieve plasma detachment at the IT but difficult to realize at the OT, with the threshold of B powder flow rate being one order of magnitude larger at the OT than at the IT. In comparison, in the $\boldsymbol{B}_{UnF}$, the outer target achieves plasma detachment first, and the B powder flow rate thresholds are similar at both the IT and OT. At the B powder injection flow rate of 1.2×10^{21} atoms/s (the injection flow rate used in discharges #85043 and #93469), the detached plasma at the inner target in $\boldsymbol{B}_{Fav}$ and reduced electron temperature at the outer target in $\boldsymbol{B}_{UnF}$ are qualitatively consistent with the above experimental results.

3.2 Particle distribution

Once the B powder is injected into the plasma, it receives the incoming energetic plasma and is ablated into neutrals. Then, these neutrals collide with the background plasma during their movement, undergoing ionizations, recombinations, and so on. These interactions not only change the distribution of the background plasma but also redistribute impurity ions. Previous studies have shown that the $\boldsymbol{E}\times\boldsymbol{B}$ drift changes the distribution of particles in the divertor region and, subsequently, affects the behaviour of the plasma detachment [42–44]. In this section, we will discuss the distribution of D ions and impurity particles, and the effects of $\boldsymbol{E}\times\boldsymbol{B}$ drift on them.

The two-dimensional distribution of all B-ions density is shown in Fig. 4. In both toloidal magnetic field directions, their distribution patterns are similar in all the cases with the same injection flow rates, and the ions are distributed mostly in the divertor region. At a low injection flow rate of 3.0×10^{19} atoms/s (Figs. 4(a) and 4(e)), impurity ions exist mainly near the injection position. When the flow rate is increased to 1.2×10^{21} atoms/s, the B ions turned to be concentrated near the separatrix in the inner divertor region. As the injection flow rate rises further to 4.0×10^{21} atoms/s, the density of impurity ions continue to increase in the inner divertor region, and in the meantime, some B ions are found to be present in the outer divertor. However, some differences between the favourable and unfavourable $\boldsymbol{B}_t$ configurations are observed: for instance, the density peak near the injection position in Fig. 4(e) is higher than that in Fig. 4(a); the high-density region near the target in Fig. 4(f) is presented mostly in the inner PFR, while that in Fig. 4(b) is in the near SOL, and more B ions turn up in the outer PFR in Fig. 4(f); the area of high-density region near the inner target in Fig. 4(g) is smaller than that in Fig. 4(c), and the density of impurity ions in the vicinity of outer target in the former is higher than in the latter. These decrpenaces are related to the different directions of $\boldsymbol{E}\times\boldsymbol{B}$ drift in $\boldsymbol{B}_{Fav}$ and $\boldsymbol{B}_{UnF}$ cases[26,45–47]. In the $\boldsymbol{B}_{Fav}$, the $\boldsymbol{E}\times\boldsymbol{B}$

drift leads to a more localized high-density cations B region near the inner target (see Figs. 4(b) and 4(d)), while in the $\boldsymbol{B}_{UnF}$, this region moves to the inner PFR (see Figs. 4(b) and 4(f)) and more B ions are driven to the outer divertor region.

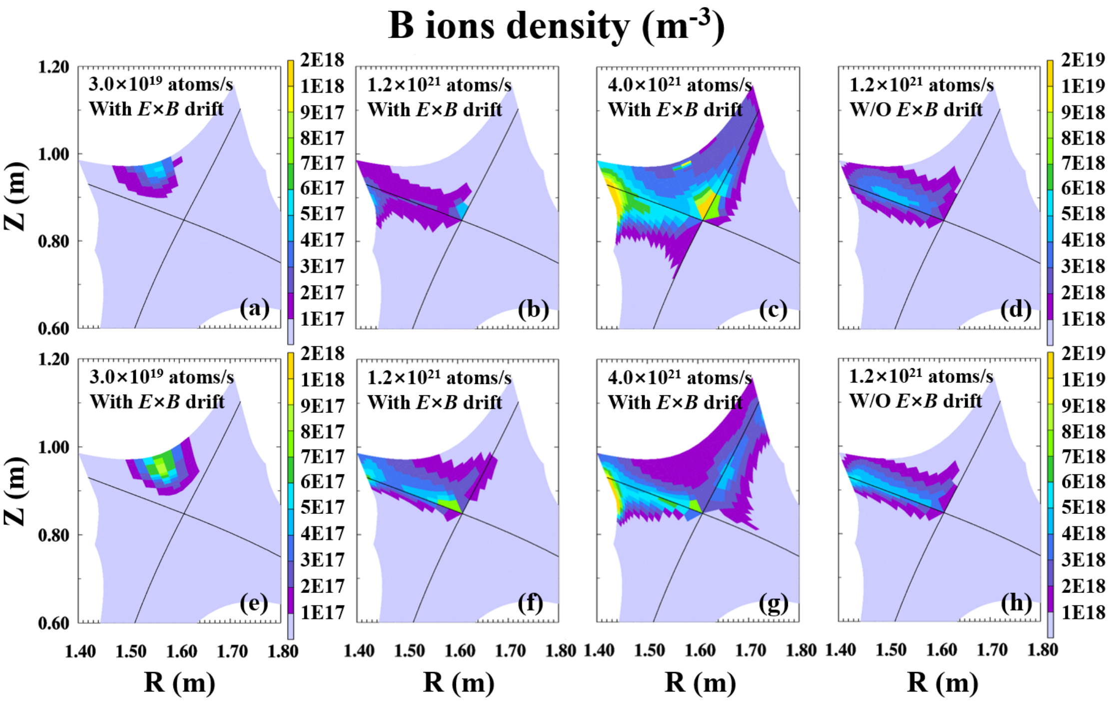

Fig. 4 Two-dimensional distribution of boron ion density in the divertor region. The top row for favourable $\boldsymbol{B}_t$ cases; the bottom row for unfavourable $\boldsymbol{B}_t$ cases.

Figure 5 shows the two-dimensional distribution of D^+ ion density in the divertor region. In the case free of impurity injection, the D^+ density is considerably higher at the inner target than at the outer target in the $\boldsymbol{B}_{Fav}$ configuration (Fig. 5(a)); while the density is noticeably higher at the outer target than at the inner target in the $\boldsymbol{B}_{UnF}$ configuration (Fig. 5(f)). These observations are consistent with both the experimental and other simulation results [42,48–51]. After the injection of B powder with a small flow rate of 3.0×10^{19} atoms/s (Fig. 5(b)), the D^+ density rises in magnitude in the vicinity of the injection position and the inner target in the $\boldsymbol{B}_{Fav}$ case. As the flow rate increases to 1.2×10^{21} atoms/s (Fig. 5(c)), the D^+ density increases significantly near the X-point and the inner target, especially in the near SOL where a broadened high-density region appears. Eventually, as the flow rate goes up to 4.0×10^{21} atoms/s (Fig. 5(d)), the D^+ density exhibits an evident increase at the outer target. In the $\boldsymbol{B}_{UnF}$ configuration, the variation of D^+ density is similar to that in the favourable $\boldsymbol{B}_t$, but the in-out divertor asymmetry of D^+ density is not as remarkable as in the latter. Comparing the cases (the B powder flow rate at 1.2×10^{21} atoms/s) with and without $\boldsymbol{E}\times\boldsymbol{B}$ drift effects, in the $\boldsymbol{B}_{Fav}$ direction (Figs. 5(c) and 5(e)), it is found that including $\boldsymbol{E}\times\boldsymbol{B}$ drift effects, the D^+ density is considerably larger near the inner target and the high-density region is wider than in the case without $\boldsymbol{E}\times\boldsymbol{B}$ drift effect; in the $\boldsymbol{B}_{UnF}$ direction (Figs. 5(h) and 5(j)), the D^+ density near the outer target is much larger when $\boldsymbol{E}\times\boldsymbol{B}$ drift effects is included. Thus, $\boldsymbol{E}\times\boldsymbol{B}$ drift in $\boldsymbol{B}_{Fav}$ exacerbates the in-out divertor asymmetry in D^+ distribution, while in $\boldsymbol{B}_{UnF}$ it mitigates the in-out divertor asymmetry in D^+ distribution.

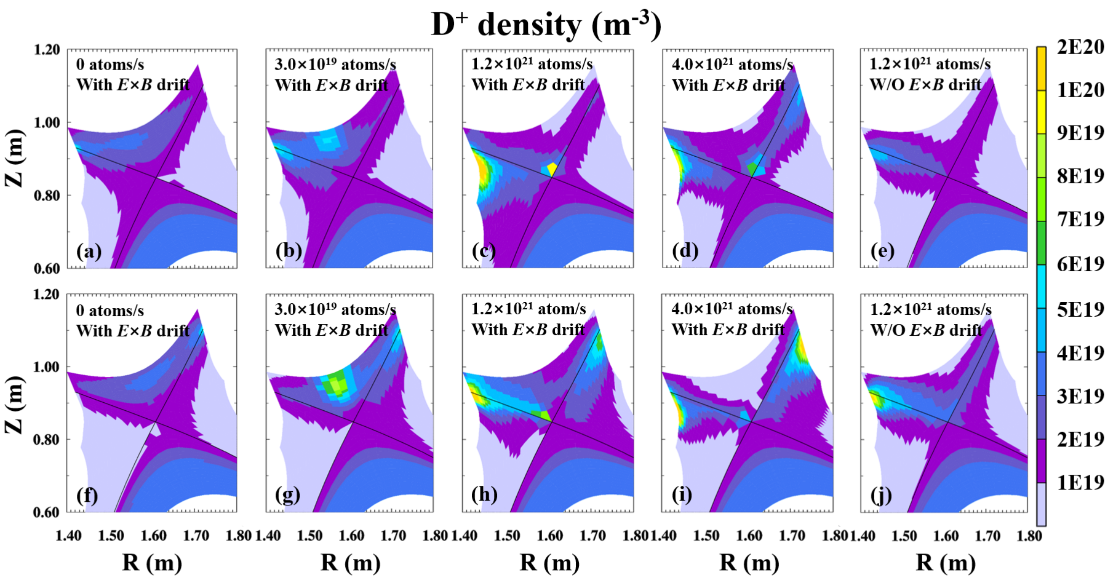

Fig. 5 Two-dimensional distribution of deuterium ion density in the divertor region. The top row for favourable $\boldsymbol{B}_t$ cases; the bottom row for unfavourable $\boldsymbol{B}_t$ cases.

From the distribution of ions, the distribution of B ions is influenced by the injection location, and the distribution of D^+ ions can be affected by the injection parameters of B powder and $\boldsymbol{E}\times\boldsymbol{B}$ drift. The details of the distribution of D^+ ions are further analysed. In SOLPS, the poloidal and radial D^+ fluxes are calculated [29,52],

$$\tilde{\Gamma}_x = \Gamma_{AN,x} + \Gamma_{para.,x} + \Gamma_{corr.,x} + \Gamma_{\boldsymbol{E}\times\boldsymbol{B},x} + \tilde{\Gamma}_{dia,x} \quad (3.1)$$

$$\tilde{\Gamma}_y = \Gamma_{AN,y} + \Gamma_{\boldsymbol{E}\times\boldsymbol{B},y} + \tilde{\Gamma}_{dia,y} + \Gamma_{curr.,y} \quad (3.2)$$

In the poloidal direction, apart from the $\boldsymbol{E}\times\boldsymbol{B}$ drift-driven ($\Gamma_{\boldsymbol{E}\times\boldsymbol{B},x}$) and diamagnetic drift-driven ($\tilde{\Gamma}_{dia,x}$)

fluxes, Γ_x also includes the anomalous diffusive flux ($\Gamma_{AN,x}$), and the poloidal component of parallel flux ($\Gamma_{para.,x}$), and the flux ($\Gamma_{corr.,x}$) from Rhie and Chow upwind correction velocity. In the radial direction, $\Gamma_{curr.,y}$ is the particle flux driven by current [29,52]. Taking the B powder flow rate of 1.2×10^{21} atoms/s in $\boldsymbol{B}_{Fav}$ as an example, the poloidal and radial D^+ fluxes and their corresponding components at the inner target are shown in Fig. 6, and Figs. 6(a) and 6(c) are for pure D discharge and Figs. 6(b) and 6(d) are for discharge with B powder injection. In pure D discharge, the poloidal D^+ flux is determined mainly by the components of parallel D^+ flux and poloidal $\boldsymbol{E}_r\times\boldsymbol{B}$ drift-driven flux, and the radial particle flux is determined primarily by anomalous diffusion and radial $\boldsymbol{E}_p\times\boldsymbol{B}$ drift. In addition,the directions of the poloidal and radial $\boldsymbol{E}\times\boldsymbol{B}$ drift components obtained in the simulation are in good agreement with other works[26,45–47]. In B powder injection discharge, the poloidal D^+ flux is governed mainly by the parallel D^+ flux; the small radial temperature gradient leads to the small radial electric field, which reduces the contribution of poloidal $\boldsymbol{E}_r\times\boldsymbol{B}$ drift to the poloidal D^+ flux. The radial D^+ flux remains determined by anomalous diffusion and radial $\boldsymbol{E}_p\times\boldsymbol{B}$ drift, both of which increase, especially the radial $\boldsymbol{E}_p\times\boldsymbol{B}$ drift. The injection of B powder directly increases the parallel D^+ flux and the radial anomalous diffusion-driven D^+ flux, and it also alters the electric field, thereby affecting $\boldsymbol{E}\times\boldsymbol{B}$ drift and leading to the redistribution of D^+ ions.

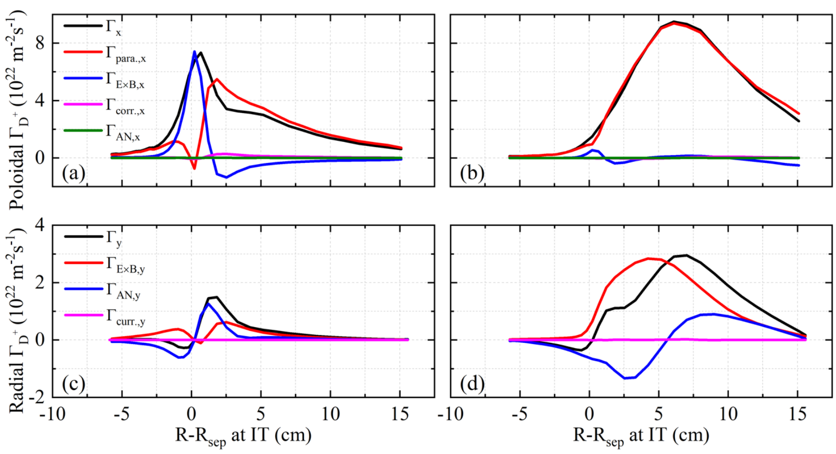

Fig. 6 The poloidal (top row) and radial (bottom row) D^+ fluxes at the inner target (IT) in favourable $\boldsymbol{B}_t$ direction. Subfigures (a) and (c) are for pure D discharge, and (b) and (d) are for discharge with boron powder flow rate of 1.2×10^{21} atoms/s.

The two-dimensional distributions of poloidal (top row) and radial (bottom row) D^+ fluxes in $\boldsymbol{B}_{Fav}$ are further presented in Fig. 7 to analyze the distribution of D^+ ions at different B injection flow rates. The positive radial D^+ flux represents particles moving from the PFR towards the SOL, and the positive poloidal D^+ flux represents particles flowing towards the inner target (as shown in Fig. 1). We discuss the $\boldsymbol{B}_{Fav}$ cases first. At the low B powder flow rate of 3.0×10^{19} atoms/s, B ions distribute mostly near the injection position (as shown in Fig. 5(a)), and the local-reduced velocity caused by B forming a localized low-poloidal D^+ flux region, as shown by the red ellipse in Fig. 7(b), which eventually leads to the accumulation of D^+ ions there. At the same time, the increased positive poloidal and radial D^+ fluxes in the vicinity of the injection location result in an enhancement in D^+ density at the inner target. At the flow rate of 1.2×10^{21} atoms/s (Fig. 6(c)), the large positive poloidal D^+ flux leads to D ions flowing into the inner divertor region, and the increased radial $\boldsymbol{E}_p\times\boldsymbol{B}$ drift (Fig. 6(d)) at the inner target enhances the local D^+ density significantly in the near-SOL. As the flow rate increases to 4.0×10^{21} atoms/s, the increase in negative poloidal D^+ flux in the outer divertor leads to noticeable D^+ (Fig. 5(d)) moving towards the outer target. In the $\boldsymbol{B}_{UnF}$, the mechanism of D^+ redistribution at the same flow rate is the same as in the $\boldsymbol{B}_{Fav}$, except that $\boldsymbol{E}\times\boldsymbol{B}$ drifts point in the opposite direction. The effect of B powder on the distribution of D^+ ions is related to both the injection location and the flow rate. As the injection location is close to inner divertor (location R_1 as shown in Fig. 1), particles are transported preferentially to the inner divertor. However, particles are also transported to the outer divertor if the injection flow rate is sufficiently large.

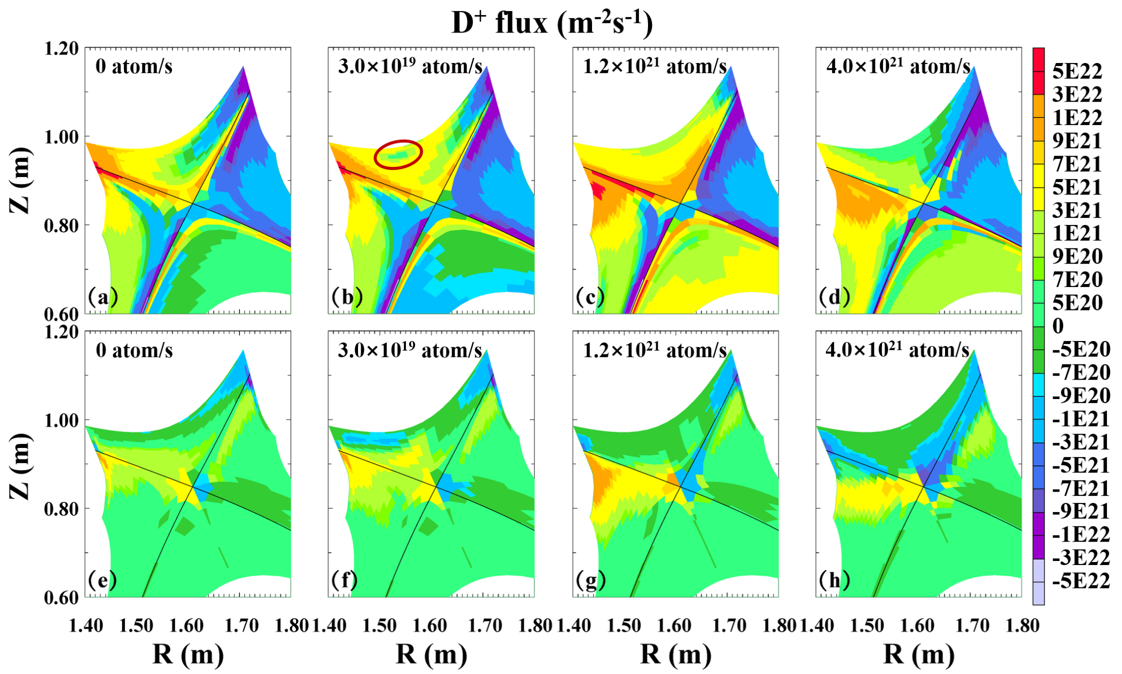

Fig. 7 Two-dimensional distribution of poloidal (top row) and radial (bottom row) D^+ fluxes in favourable $\boldsymbol{B}_t$ direction. The positive radial D^+ flux represents particles moving from the PFR towards the SOL, and the positive poloidal D^+ flux represents particles flowing towards the inner target.

From the above results, no matter whether the discharge is in the direction of either $\boldsymbol{B}_{Fav}$ or $\boldsymbol{B}_{UnF}$, the injection parameters of B powder and $\boldsymbol{E}\times\boldsymbol{B}$ drift have a large effect on the distribution of D^+ and impurity ions in the divertor region. In the favourable $\boldsymbol{B}_t$ with B flow rate of 1.2×10^{21} atoms/s, both the $\boldsymbol{E}\times\boldsymbol{B}$ drift and the injection location are beneficial to the particle accumulation in the inner divertor, resulting in a broadened high-density region near the inner target and a large in-out divertor asymmetry. In contrast, in the unfavourable $\boldsymbol{B}_t$, the $\boldsymbol{E}\times\boldsymbol{B}$ drift causes the particles accumulation in the outer divertor while the injection location favours particle accumulation in the inner divertor; their competition with comparable particle-driving capabilities leads to a weak in-out divertor asymmetry. This is one of the reasons why there are different degrees of in-out divertor asymmetry in both $\boldsymbol{B}_t$ directions and different B powder thresholds for plasma detachment. In Fig. 3, a bulge appears in each temperature and heat flux profiles at the outer target as the B impurity flow rate increases. The occurrence of the bulge may be associated with $\boldsymbol{E}\times\boldsymbol{B}$ drift and the B powder injection location. When the B flow rate is small (for instance, 3.0×10^{19} atoms/s), the impurity density is higher next to the injection position than other regions and the D^+ density is also slightly higher (owing to the localized low-poloidal D^+ flux), as shown in Figs. 4(e) and 5(g). In the meantime, the ***E***×***B*** drift drives D^+ ions to move towards the outer divertor and enhance the density of D^+ there as shown in Fig. 5(g). When the B impurity flow rate exceeds 4.0×10^{20} atoms/s, injection location first leads to the movement of the particles to the inner divertor, as shown in Fig. 5(h). This movement reduces the influx to the outer divertor, leading to a drop each in both electron density and radiation power near the outer target and subsequently, resulting in a rise in both T_e and q_t. However, the particle flux rises in Fig. 3(d) when B impurity flow rate exceeds 4.0×10^{20} atoms/s (which may be caused by the poloidal velocity). Eventually, the large flow rate of B powder causes the particles to the outer divertor, and therefore the temperature and heat flux at the outer target decreases again, which is the reason for the occurrence of bulges as shown in Fig. 3.

3.3 Radiation

Both experimental and simulation results show a significant change in target electron temperature after B powder injection. For discharges involving impurity injection, the simple two-point model [53] is not adequate anymore; therefore the modified two-point model [53,54] is used to analyse the plasma detachment process. Equation 3.3 is used to describe the electron temperature at the target,

$$T_{et} = \frac{q_\parallel^2}{n_{eu}^2}\left(\frac{2\kappa_e}{7q_\parallel L_\parallel}\right)^{4/7}\frac{2m_i}{\gamma^2 e^2}\frac{(1-f_{pow})^2}{(1-f_{mom})^2(1-f_{conv})^{4/7}}, \tag{3.3}$$

Here f_{pow}, f_{mom}, and f_{conv} are the energy and momentum loss fractions, and the heat convection fraction, respectively. The equation indicates that energy and momentum losses have greater impact on the target temperature than heat convection. Thus, we focus our discussion on the energy and momentum loss. From equation 3.3, the increasing energy loss causes a decrease in electron temperature, while an increase in momentum loss leads to an increase in electron temperature. Therefore, the energy loss is the main reason for the decrease in temperature. Table 1 summarizes the radiation powers of individual regions (as shown in Fig. 1) in four cases: Case I (without ***E***×***B*** drift in $\boldsymbol{B}_{Fav}$), Case II (without ***E***×***B*** drift in $\boldsymbol{B}_{UnF}$), Case III (with ***E***×***B*** drift in $\boldsymbol{B}_{Fav}$), Case IV (with ***E***×***B*** drift in $\boldsymbol{B}_{UnF}$); and the two-dimensional distributions of D (top row), B (middle row) and D plus B (bottom row) radiation powers for each case are shown in Fig. 8. Either D or B radiation includes the line, bremsstrahlung and neutral radiations.

In this section, the B flow rates in all cases are chosen to be 1.2×10^{21} atoms/s. The different radiation powers in specific regions of cases I and II are due to the differences in the radial particle and thermal diffusivities. From Table 1, we know that most of the powers are radiated in the divertor region for these four cases, accounting for about 95%, 97%, 94% and 96% of the total radiation powers, respectively, for Case I, II, III and IV. The radiation powers of two pairs (inner divertor in $\boldsymbol{B}_{Fav}$ and outer divertor in $\boldsymbol{B}_{UnF}$, outer divertor in $\boldsymbol{B}_{Fav}$ and inner divertor in $\boldsymbol{B}_{UnF}$) with $\boldsymbol{E}\times\boldsymbol{B}$ drift are compared, and the directions of $\boldsymbol{E}\times\boldsymbol{B}$ drift are the same for each pair. The radiation powers in OD in $\boldsymbol{B}_{UnF}$ is 308 kW smaller than that in ID in $\boldsymbol{B}_{Fav}$, and the high-radiation region of the latter is close to the inner target (see Fig. 8(j)), while that of the former is close to the X-point (see Fig. 8(l)). As a result, plasma detachment is achieved at the inner target in $\boldsymbol{B}_{Fav}$, whereas in $\boldsymbol{B}_{UnF}$, at the outer target the plasma still is in attached state, although a considerable temperature drop is observed. The radiation power in the ID in $\boldsymbol{B}_{UnF}$ is 2.7 times higher than that in the OD in $\boldsymbol{B}_{Fav}$, and such a high power results in a significant decrease in temperature at the inner target to 17 from 60 eV, a reduction by ~72%. In contrast, in $\boldsymbol{B}_{Fav}$ the temperature at the outer target drops from 54 to 34 eV, a reduction by ~37%. Including the effect of $\boldsymbol{E}\times\boldsymbol{B}$ drift in the $\boldsymbol{B}_{Fav}$, the radiation power decreases from 609 to 356 kW in the inner divertor, while it increases from 223 to 280 kW in the outer divertor. Similar change trends are also observed in cases in the $\boldsymbol{B}_{UnF}$, but with various magnitudes. As can be seen in Fig. 8, the power radiated by species B is much greater than by species D; therefore, the reduction of radiation power in the inner divertor region (as shown in table 1) is actually caused mainly by the B impurity. In the favourable $\boldsymbol{B}_t$, although the radiation in the inner divertor (in the vicinity of the separatrix and inner PFR) is smaller when considering $\boldsymbol{E}\times\boldsymbol{B}$ drift, the radiation becomes intensified in the near-SOL (see Figs. 8(e) and (f)). The intense radiation in the localized region in the inner divertor gives a reasonable explanation why the inner target achieves plasma detachment more easily. In the unfavourable $\boldsymbol{B}_t$, the radiation power turns relatively weaker in the inner divertor region (especially in the PFR) and stronger in the outer divertor region after considering $\boldsymbol{E}\times\boldsymbol{B}$ drift; and the reason for the radiation change will be analyzed later.

Table 1. The radiation powers in individual regions: the core, SOL, inner divertor (ID), and outer divertor (OD) regions, as well as the total of all regions. The B injection flow rate is 1.2×10^{21} atoms/s and the unit is in kW.

	CORE	SOL	OD	ID	Total
Case I (W/O $\boldsymbol{E}\times\boldsymbol{B}$ in $\boldsymbol{B}_{Fav}$)	27	17	223	609	876
Case II (W/O $\boldsymbol{E}\times\boldsymbol{B}$ in $\boldsymbol{B}_{UnF}$)	22	14	282	906	1223
Case III (with $\boldsymbol{E}\times\boldsymbol{B}$ in $\boldsymbol{B}_{Fav}$)	24	17	280	356	677
Case IV (with $\boldsymbol{E}\times\boldsymbol{B}$ in $\boldsymbol{B}_{UnF}$)	30	18	308	762	1118

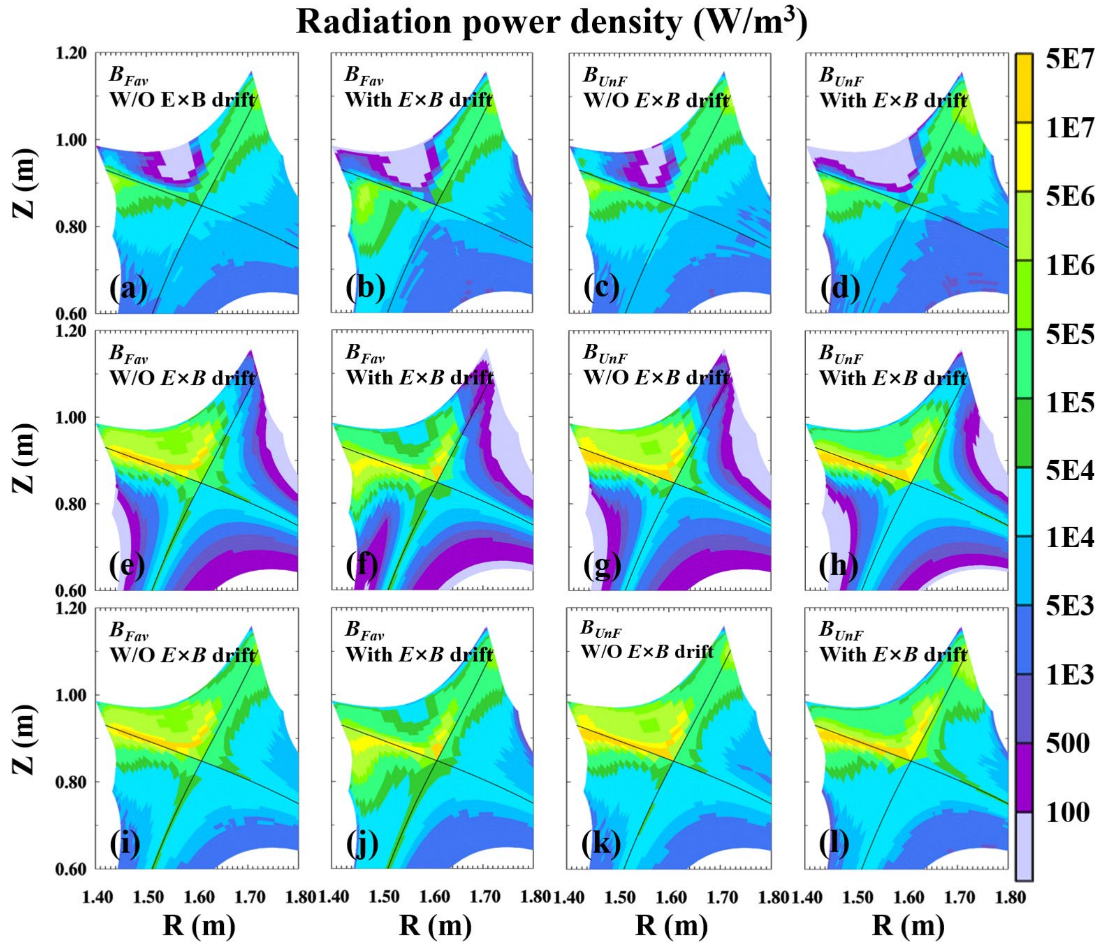

Fig. 8 Distribution of radiation power density in favourable and unfavourable $\boldsymbol{B}_t$ directions. Top, middle and bottom rows are for the radiation power density of D, B and D plus B, respectively. The B powder flow rate is 1.2×10^{21} atoms/s.

The role of impurity ions in radiation power varies in discharges. Figure 9 shows a histogram of radiation power contributed by different B ions in the $\boldsymbol{B}_{Fav}$ and $\boldsymbol{B}_{UnF}$ directions (B powder flow rate, 1.2×10^{21} atoms/s). The radiation powers in the $\boldsymbol{B}_{UnF}$ are larger than those in the $\boldsymbol{B}_{Fav}$, which is consistent with Table 1. The power radiated by cations B^{1+} and B^{2+} accounts for most of the total impurity radiation for the favourable (95.3%) and unfavourable (94.8%) $\boldsymbol{B}_t$ directions.

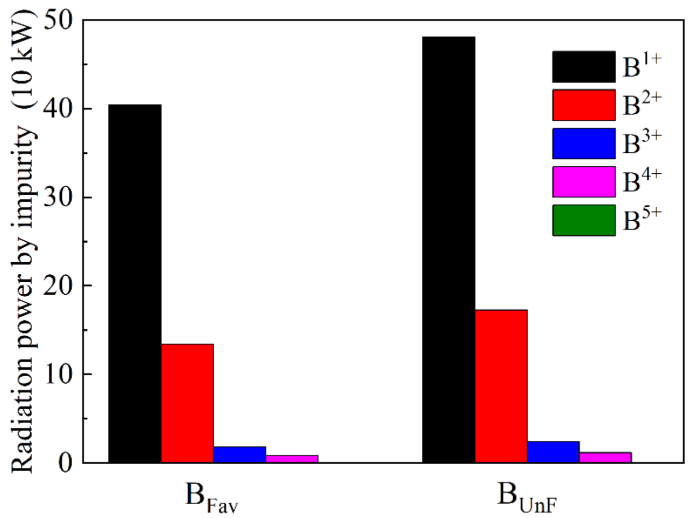

Fig. 9 Radiation power by impurity ions for the favourable and unfavourable $\boldsymbol{B}_t$ directions with including $\boldsymbol{E}\times\boldsymbol{B}$ drift effect. The B powder flow rate is 1.2×10^{21} atoms/s.

The radiation power caused by impurity in plasma can be evaluated by the formula, $P_{rad} = n_e \sum_Z n_Z \sum_Z (\xi_Z L_Z(T_e))$, where n_e and n_Z represent electron density and impurity density, respectively, ξ_Z represents the relative density of different impurity charge states, and $L_Z(T_e)$ is the cooling factor, which describes the temperature-dependent radiation capacity of an impurity [55]. When electron temperature T_e is in the range from 1 to 10 eV, the cooling factor of B impurity is relatively much larger. When T_e is higher than 10 eV, the cooling factor maintains a small change in magnitude [14]. In the plasma, the temperature in the PFR (both in the favourable and unfavourable $\boldsymbol{B}_t$ directions) and near the inner target (plasma detachment achieved in the favourable $\boldsymbol{B}_t$) more or less falls into the temperature range (1~10 eV); therefore, the relatively high cooling factor leads to stronger radiation in this region.

The distribution of electron density is more or less close to the D^+ ions density. The distributions of D and B ions have been discussed in section 3.2. In the $\boldsymbol{B}_{Fav}$, the densities of both B and D ions are much higher in the region near the inner target (Figs. 4(b) and 5(c)), especially in the near-SOL, give rise to strong radiation there and subsequently cools the plasma therein. As the temperature drops down to 1~10 eV, the cooling factor becomes larger, and thus the radiation continues to be strengthened (forming the localized high radiation region as shown in Fig. 8(f)), and the plasma temperature continues to fall until plasma detachment is achieved. As for the outer divertor, the strengthened impurity radiation is related to higher impurity ions (as shown in Fig. 4(b)) and D ions (electrons) (Fig. 5(c)) near the separatrix and X-point. The temperature dropped only to 34 eV (Fig. 3) due to the high background temperature at the outer target. The combination of different radiation distributions in the inner and outer divertor regions, and high background temperature at the outer target and low background temperature at the inner target results in a significant in-out asymmetry in temperature (as shown in Fig. 3). In the unfavourable $\boldsymbol{B}_t$, injection location causes particles to flow towards the inner divertor, while the $\boldsymbol{E}\times\boldsymbol{B}$ drift drives particles to the outer divertor. These factors lead to an enhancement in electron, B and D ions densities in the outer divertor, and hence the radiation becomes weaker in the inner divertor and stronger in the outer divertor (however, the total radiation power in the inner divertor is still more than twice larger that in the outer divertor), as shown in Table 1. As a result, strong radiation but the relatively high electron temperature at the inner target and relatively weak radiation but low temperature at the outer target leading to a moderate in-out temperature asymmetry.

3.4 Different impurity injection locations

The impurity injection location has an influence on the distribution of impurity particles and background plasma. The injection results at R_1=1.570 m presented above show that impurity injection causes significant particle accumulation in the inner divertor region. Considering the impurity injection method and the higher electron temperature at the outer target with the favourable $\boldsymbol{B}_t$, two other positions R_2=1.730 m and R_3=1.945 m (as shown in Fig. 1) are also selected for impurity injection simulation in the favourable $\boldsymbol{B}_t$. Apart from the impurity injection position, other parameters are kept the same for all the scenarios. In each position, we choose two typical flow rates of B powder injection: 1.2×10^{21} atoms/s (which was used in the experiments [23]) and 4.9×10^{21}, 4.0×10^{21} and 3.7×10^{21} atoms/s for R_1, R_2 and R_3 cases, respectively, which are the B injection flow rate threshold for plasma detachment at the outer target.

The effects of impurity B injection at different locations on the target electron temperature and heat flux are discussed first. The target profiles, as shown in Fig. 10, indicate that when the B powder flow rate is 1.2×10^{21} atoms/s, the temperature and heat flux at the inner target in case at location R_1 decreases most significantly, achieving plasma detachment state. At the location R_2, in contrast, both the heat flux and temperature peaks remain high compared with the other locations. At the outer target, both the temperature and heat flux are at a high level for any of the three injection locations. In addition, it is worth noting that when B powder injected at location R_2, there exists a localized, low-magnitude region either in temperature or in heat flux in the SOL region. To see the impact of impurity particles on the upstream, the electron density, electron temperature and effective charge number Z_{eff} at the outer mid-plane for three injection locations are presented in Fig. 11, in which the B powder flow rates are all the same, 1.2×10^{21} atoms/s. As can be seen from Figs. 11(a) and 11(b), the effects of B injection at all locations are small on the upstream density and temperature profiles, although the increase in electron density at the location R_3 is the most noticeable. Correspondingly, the impurity density at the R_3=1.945 m case is the highest in the core region with Z_{eff} reaching up to 1.4 at the separatrix, which is still at a low level of effective charge number in the EAST experiments [56]. Thus, we may conclude that the B ions do not bring noticeable deleterious effects to the core plasma confinement at the B powder injection rate of 1.2×10^{21} atoms/s.

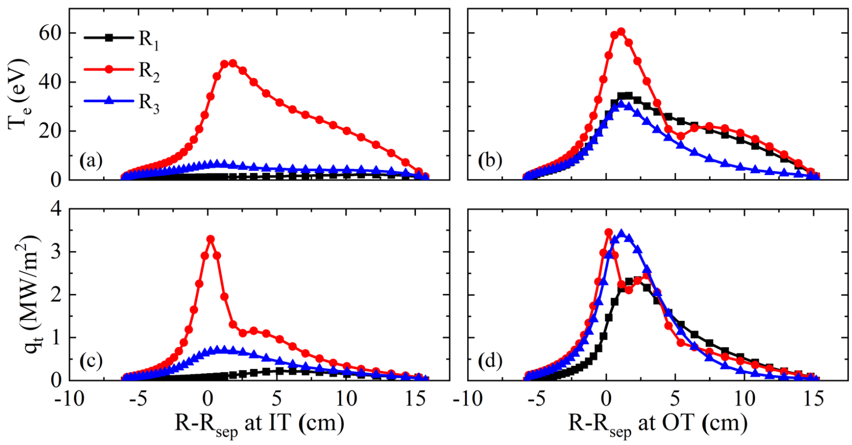

Fig. 10 Electron temperature and perpendicular energy flux density at the inner and outer targets in cases with B injection at locations R_1, R_2 and R_3. The B powder flow rate of 1.2×10^{21} atoms/s.

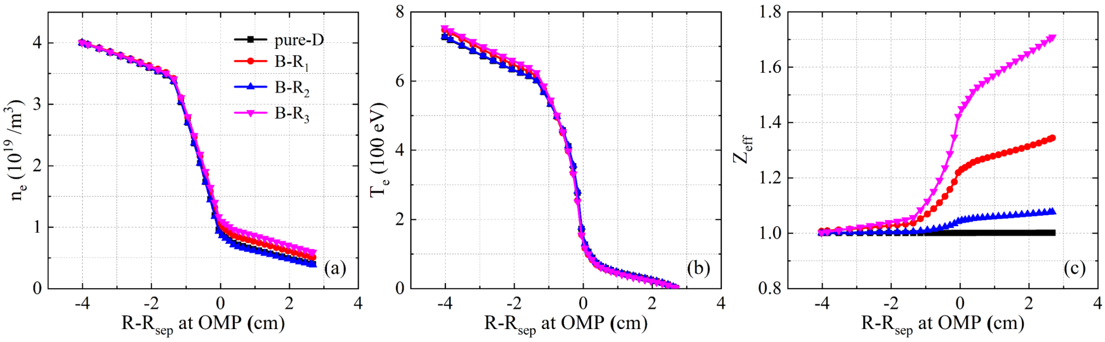

Fig. 11 Electron density (a), electron temperature (b) and effective charge number (c) profiles at the outer mid-plane in cases of no B powder (pure-D) injectoion and B powder injection at locations R_1, R_2 and R_3, with a B flow rate of 1.2×10^{21} atoms/s.

The radiation powers of impurity ions of different charged states are shown in Table 2, and the main impurity radiation contributors are always B^{1+} and B^{2+} regardless of the injection position; thus, these two types of particles are of main interest in the following. In addition, an important finding is that at R_2=1.730 m, the radiation power of B^{1+} and B^{2+} is much smaller than that at the other two injection positions with B powder flow rate of 1.2×10^{21} atoms/s. When the B powder flow rate is raised to 4.0×10^{21} atoms/s, the radiation powers of B^{1+} and B^{2+}, respectively, rise up remarkably; plasma detachment is achieved at the outer target. The radiation powers of each region and the whole domain are summarized in Table 3, and from it we can see that at the flow rate of 1.2×10^{21} atoms/s the maximal radiation power of the whole domain (677 kW) occurs in the case with injection position at R_1=1.570 m, the intermediate radiation power (543 kW) appears in the case with R_3=1.945 m, and in the case with R_2=1.730 m, B impurity dissipates the least power (135 kW). The radiation of the R_1 case is mainly concentrated in the divertor region and the radiation power in the inner divertor region is larger than the outer divertor region owing to the accumulation of B and D species in the inner divertor region. The radiation power of the R_2 case is only 34 kW in the inner divertor region, which is similar to the radiation power without powder injection. The radiation power of R_3 case is significantly higher in the SOL, which implies that the incoming energy flux from the upstream is reduced effectively. In addition, the detachment threshold at the outer target for R_2=1.730 m is similar to R_3 and smaller than R_1, and the radiation for detachment threshold increases dramatically compared to the flow rate of 1.2×10^{21} atoms/s, indicating that the injection location at R_2=1.730 m is sensitive to the B powder flow rate.

Table 2. The radiation powers of impurity ions corresponding to three injection positions. The power is in unit of kW, and the flow rate is in unit of 10^{21} atoms/s.

Location (flow rate)	B^{1+}	B^{2+}	B^{3+}	B^{4+}	B^{5+}
R_1 (1.2)	404	134	18	8	0.040
R_1 (4.9)	616	253	53	28	0.2
R_2 (1.2)	30	11	3	1	0.007
R_2 (4.0)	269	167	20	10	0.04
R_3 (1.2)	152	103	32	15	0.056
R_3 (3.7)	510	347	106	46	0.2

Table 3. The radiation powers (including all types of B species and background D) of each individual region and whole domain (TOTAL). CORE, SOL, OD and ID represent the core region, SOL, outer and inner divertor regions, respectively. The power is in unit of kW, and the flow rate is in unit of 10^{21} atoms/s.

Location (flow rate)	CORE	SOL	OD	ID	TOTAL
No powder	8	6	37	42	93
R_1 (1.2)	24	17	280	356	677
R_1 (4.9)	65	64	493	343	965
R_2 (1.2)	11	7	83	34	135
R_2 (4.0)	26	38	767	32	863
R_3 (1.2)	36	309	124	74	543
R_3 (3.7)	99	611	292	8	1010

From the above results, it can be seen that when the flow rate of B powder is 1.2×10^{21} atoms/s, the B powder injected at R_1 has the most radiation power in the whole region and at this injection location it is the easiest to achieve plasma detachment at the inner target. The B powder injection at the R_3 position results in a little more radiation in the inner and outer divertor regions, compared with the case without

B injection; in contrast, much more power is radiated in the SOL. In the R_2 case, although B powder is injected from the vicinity of the outer strike point, its effects on the outer target is not significant at the current flow rate. The background plasma responses at the three injection locations are closely related to the distribution of impurity. The density distributions of B^{1+} and B^{2+} in Fig. 12 show that they are different significantly in the four cases: in the R_1 case, the impurity ions are concentrated along the separatrix in the inner divertor region; in the R_2 case with flow rate of 1.2×10^{21} atoms/s, the impurities are concentrated in a localized area near the injection position, and with 4.0×10^{21} atoms/s, the impurity is spread almost throughout the entire outer divertor region, with some leakage into the upstream; and in the R_3 case, the impurity has diffusive stretch along the poloidal direction in the vicinity of the injection position. The distribution of impurity particles in R_2 case with flow rate of 1.2×10^{21} atoms/s is more specific and is localized only in a very small region near the injection location, which is one reason for the localized drop in temperature and heat flux at the outer target in Fig. 10.

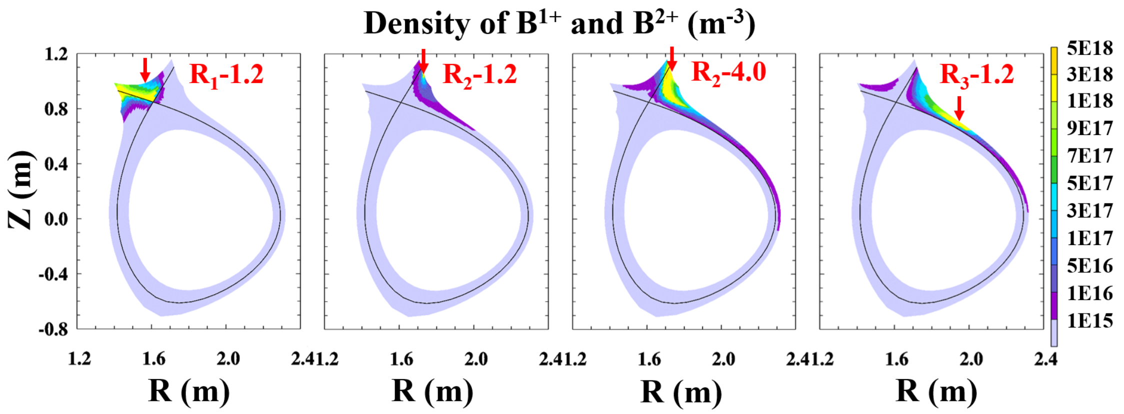

Fig. 12 The density distribution of combining ions B^{1+} and B^{2+} in cases of R_1, R_2 and R_3 injection locations. The B powder flow rates are 1.2×10^{21} (R_1), 1.2×10^{21} and 4.0×10^{21} (R_2), and 1.2×10^{21} atoms/s (R_3).

The electron temperature is distinctively differences in the regions next to the different injection locations. The ionization threshold for B atoms, B^{1+} and B^{2+} are, respectively, 8.3, 25.2 and 37.9 eV. Therefore, they exist only in low temperature regions. In either the R_1 (PFR) or the R_3 (SOL) case, the electron temperature is lower than that in the R_2 case in the region where the B powder is injected. As is known, the distribution of ions B is related to the ionization mean free path of atoms B

$\lambda = v / (n_e < \sigma v >_{ion})$ [57,58], in which, v represents the average velocity of B atoms, n_e is the electron density, and $<\sigma v>_{ion}$ denotes the ionization rate coefficient of impurity atoms. As the average atomic velocities and electron densities are similar for the different injection locations, their differences are therefore negligible. As a result, the ionization mean free path is determined mainly by the ionization rate coefficient, which depends strongly on the local plasma temperature. Here the data of ionization rate coefficient was taken from the ADAS database[32]. In case with B (1.2×10^{21} atoms/s) injected at location R_2, the electron temperature near the injection location is ~15 eV (only near the injection location, and surrounded by higher temperature plasma), while it is ~1.0 eV for the other two cases with injection location at R_1 and R_3. According to the ionization rate coefficients, the ionization mean free path of B atoms in case with location R_2 is about 4 orders of magnitude shorter than that in the other two cases. Thus, the B atoms in case at R_2 exist in a small localized region. Eventually, ions B^{1+} and B^{2+} are present only in a small region due to the high temperature around the injection location. As the B injection flow rate is increased to 4.0×10^{21} atoms/s, the reduced temperature at the outer target increases the ionization mean free path; consequently, a relatively extensive distribution of B ions is present in the outer divertor (as shown in Fig. 12).

Boron particles depositing on plasma-facing walls have a considerable effect on wall condition. The flux of all B ions past the boundary of quadrilateral meshes (Fig. 1) is summarized in Table 4. The fluxes to both the inner and outer targets are in the poloidal direction and that to the dome and first wall are in the radial direction. In the R_1 cases, B particles deposit first on the inner target when the B powder flow rate is 1.2×10^{21} atoms/s; when the flow rate is raised to 4.9×10^{21} atoms/s, part of the B particles are transported to the outer divertor, and deposit there. In the R_2 cases, B particles deposit mainly on the outer target. In the R_3 cases, B particles deposit mainly on the outer target and part of the first wall. These show that the whereabouts of the deposition of impurity B is strongly related to the injection location. Thus, for the purpose of wall conditioning, it is important to select the injection location.

Table 4. All B ions flux passing through the boundary. FIT and FOT denote, respectively, the fluxes of B ions to the inner and the outer targets; FDOM denotes the flux of B ions to the dome; FFW denotes the flux of B ions to the first wall. The flow rate is in unit of 10^{21} atoms/s, and the ion flux unit is 10^{19} /s.

Location (flow rate)	FIT	FOT	FDOM	FFW
R_1 (1.2)	89.4	4.4	0.7	9.4
R_1 (4.9)	188.2	120.3	4.3	25.3
R_2 (1.2)	0.5	109.9	0.1	2.4
R_2 (4.0)	7.7	217.3	3.2	14.7
R_3 (1.2)	4.3	68.6	0.9	23.5
R_3 (3.7)	18.1	223.1	5.3	49.8

Comparing different injection positions, we can know that B powder injected from position R_1 favors plasma detachment at the inner target; from position R_3, it is conducive to radiating power in the SOL, but has a relatively big impact on the core region; and from position R_2 it makes plasma detachment at the outer target slightly easier than from the R_1 but the heat flux to the outer target is more sensitive to the B powder flow rate. The different performances of the three injection locations are related to the electron temperature in the vicinity of the injection position. The deposition position of B particles is strongly correlated to their injection location and they deposit preferentially on the wall with strong plasma-wall interaction, i.e., on divertor targets, and similar findings have been observed in ASDEX Upgrade[16].

4. Discussion

The influence of $\boldsymbol{E}\times\boldsymbol{B}$ drift and injection position on divertor plasma properties has been studied in experiments [47,59,26] and simulations [36,60] . The effect of $\boldsymbol{E}\times\boldsymbol{B}$ drift on divertor plasma properties has been investigated by Xu et al [47] and Jia et al [36]. Both works indicate that $\boldsymbol{E}\times\boldsymbol{B}$ drift led to the redistribution of plasma particles in the divertor regions: radial $\boldsymbol{E_p}\times\boldsymbol{B}$ drift large enough produced a broadened high-density region; strong poloidal $\boldsymbol{E_r}\times\boldsymbol{B}$ drift drove plasma to form a significant particle sink. The conclusions reached in section 3.2 are consistent with these results, and the direction of $\boldsymbol{E}\times\boldsymbol{B}$ drift obtained in the present work is in good agreement with Xu's work. All of these studies show that $\boldsymbol{E}\times\boldsymbol{B}$ drift played an important role in determining the properties of divertor plasma.

Meng et al performed the experiments with different injection positions of Ne-D_2 seeding in the USN

$\boldsymbol{B}_{Fav}$ discharge on EAST device [59]. The upstream injection location in the lower outer divertor plate is similar to the location R_3 in the present work, and the downstream injection position in the upper outer divertor plate is the same as the location R_2 in this work. Their experiments indicated that a higher portion of the injected neon might enter the core when the impurity was seeded from the upstream injection location, while a higher portion remained in the upper divertor when seeded from the downstream injection position; similar results were obtained in a simulation work for a discharge scenario in future device CFETR [60]; the simulation results in the present work are consistent with these conclusions, as shown in Figs. 10 and 11. All these results indicate that the impurity injection position is an important factor affecting the plasma temperature and the heat flux to the divertor targets, which needs to be studied further. Neon seeding at the X-point, similar injection position as R_1, was simulated in the lower single null configuration for both favourable and unfavourable $\boldsymbol{B}_t$ directions[61]. The significant difference in in-out asymmetry between $\boldsymbol{B}_{Fav}$ and $\boldsymbol{B}_{UnF}$ found in the Ne-seeding simulations was similar to the results in the present work. In the Ne-seeding cases, it was observed that the radiation powers in the core and SOL regions were larger than in the divertor region; thus, plasma detachment at the target was realized mainly due to the radiation-reduced heat flux flowing into the divertor region. In contrast, the radiation caused by B powder is concentrated in the inner and outer divertor regions. This considerable difference results partly from the different radiation properties of B and Ne: the highest part of B cooling factor falls in the temperature range of 1~10 eV, existing mainly in divertor region; for Ne, it occurs in the temperature range of 10-100 eV, present mainly in the upstream near the separatrix [62]. In addition, Ne impurity was easily present in the upstream and SOL in the Ne-seeding cases, which was also one important factor for its high radiation in the upstream; in comparison, B impurity stays dominantly in the divertor region. The preliminary comparison between B and Ne impurities shows that B has less detrimental effect on the energy confinement. Deep understanding requires more devoted studies.

5. Summary and conclusions

Plasma detachment and the role of $\boldsymbol{E}\times\boldsymbol{B}$ drift were investigated during real-time B powder injection in both the favourable and unfavourable toroidal magnetic fields ($\boldsymbol{B}_{Fav}$ and $\boldsymbol{B}_{UnF}$) based on EAST discharge #85043, using the edge plasma code SOLPS-ITER. The simulated results showed that the plasma detachment at inner target in the favourable $\boldsymbol{B_t}$ and the reduced temperature at outer target in the unfavourable $\boldsymbol{B_t}$ during B powder injection were qualitatively consistent with experimental results. The important findings of this study are that B powder could reduce effectively the heat flux to the divertor targets and facilitate plasma detachment, and that there was a big difference in the B powder thresholds for plasma detachment in the $\boldsymbol{B}_{Fav}$ and $\boldsymbol{B}_{UnF}$ directions. The paper then focused on exploring the reasons for plasma detachment and the different thresholds. Detailed findings are summarized in the following.

In the discharge with favourable $\boldsymbol{B_t}$ direction, the detachment took place first at the inner target when the B powder flow rate is at 2.0×10^{20} atoms/s, and as the B powder flow rate was raised to 4.9×10^{21} atoms/s, the detachment also happened at the outer target. In contrast, with $\boldsymbol{B}_{UnF}$ direction the inner and outer targets achieved plasma detachment at similar thresholds, with the B powder flow rate of 4.2×10^{21} atoms/s for the inner target and 2.5×10^{21} atoms/s for the outer target, respectively.

Detailed analyses were then undertaken on the discharges with the B powder flow rate of 1.2×10^{21} atoms/s for both $\boldsymbol{B}_{Fav}$ and $\boldsymbol{B}_{UnF}$ directions. It was found that the in-out divertor asymmetry in B_{Fav} was considerably more severe than that in $\boldsymbol{B}_{UnF}$. In the $\boldsymbol{B}_{Fav}$, the poloidal $\boldsymbol{E_r}\times\boldsymbol{B}$ drift drove the particles from the outer divertor to the inner divertor through the private flux region, and the injection location also pushed the particles to the inner divertor. Radial $\boldsymbol{E_p}\times\boldsymbol{B}$ drift subsequently drove the particles to the SOL, leading to the formation of a broadened high-density region near the inner target, which led to intense radiation in the local region, and facilitated the plasma detachment at the inner target (correspondingly, a low B powder flux rate could lead to detachment). The combination of different radiation patterns in the inner and outer divertor regions, and high background temperature at the outer target and low background temperature at the inner target resulted in a significant in-out divertor asymmetry. In the $\boldsymbol{B}_{UnF}$ directions, the injection location resulted in particles flow to the inner divertor, while the $\boldsymbol{E}\times\boldsymbol{B}$ drift drove particles to the outer divertor. As a result, strong radiation but relatively high temperature of plasma at the inner target, and relatively weak radiation but low temperature at the outer target leading to a moderate in-out divertor asymmetry and similar B powder thresholds for detachment at the inner and outer targets.

The comparison of cases at three injection positions of interest showed that the impurity injection location at X-point resulted in dense impurity particles on the high field side of both toroidal magnetic directions, and the main impurity radiation ions were always B^{1+} and B^{2+} regardless of the injection position. The injection location at the upstream had the largest impact on the core region compared to the other two locations. In addition, an important finding was that the deposition area of particles after B injection is related to the injection location and impurity deposit preferentially on the wall with strong plasma-wall interaction. The study of different B powder injection locations provides a reference for boronizing the plasma-facing wall of future fusion devices.

Acknowledgements

This work is supported by the National Natural Science Foundation of China under Grant No. 12275040, the National Key R&D Program of China under Grant Nos. 2019YFE03030004 and Nos. 2024YEF03000200, and Users with Excellence Program of Hefei Science Center CAS (2020HSC-UE010). This research is also sponsored in part by the U.S. Department of Energy under contracts DE-AC02-09CH11466. The authors thank Supercomputing Center of Dalian University of Technology for providing part of computational resources. The views and opinions expressed herein do not necessarily reflect those of the ITER Organization.

References

[1] Shimada M. et al 2007 Nucl. Fusion 47 S1–17
[2] Pitcher C.S. et al 1997 Plasma Phys. Control. Fusion 39 779–930
[3] Loarte A. et al 2007 Nucl. Fusion 47 S203–63
[4] Pitts R.A. et al 2019 Nucl. Mater. Energy 20 100696
[5] Krasheninnikov S.I. et al 2016 Phys. Plasmas 23 055602
[6] Ryter F. et al 2013 Nucl. Fusion 53 113003
[7] Greenwald M. et al 1988 Nucl. Fusion 28 2199–207
[8] Li K. et al 2020 Plasma Phys. Control. Fusion 62 095025
[9] Reinke M.L. et al 2011 J. Nucl. Mater. 415 S340–4
[10] Kubo H. et al 2003 J. Nucl. Mater. 313–316 1197–201
[11] Laguardia L. et al 2017 Nucl. Mater. Energy 12 261–6
[12] Peng L. et al 2021 Nucl. Mater. Energy 26 100937
[13] Pigarov A.Yu. 2017 Phys. Plasmas 24 102521
[14] Effenberg F. et al 2022 Nucl. Fusion 62 106015
[15] Bortolon A. et al 2019 Nucl. Mater. Energy 19 384–9
[16] Lunsford R. et al 2019 Nucl. Fusion 59 126034
[17] Bortolon A. et al 2020 Nucl. Fusion 60 126010
[18] Gilson E P. et al 2021 Nucl. Mater. Energy 28 101043
[19] Nespoli F. et al 2020 Nucl. Mater. Energy 25 100842

[20] Lunsford R. et al 2022 Nucl. Fusion 62 086021
[21] Kawate T. et al 2022 Nucl. Fusion 62 126052
[22] Nespoli F. et al 2022 Nat. Phys. 18 350–6
[23] Sun Z. et al 2021 Nucl. Fusion 61 014002
[24] Xu W. et al 2021 Phys. Scr. 96 124034
[25] Du H. et al 2017 Nucl. Fusion 57 116022
[26] Liu J B. et al 2019 Nucl. Fusion 59 126046
[27] Wang Y. et al 2023 Nucl. Fusion 63 096024
[28] Maingi R. et al 2020 J. Fusion Energy 39 429–35
[29] Schneider R. et al 2006 Contrib. Plasma Phys. 46 3–191
[30] Chankin A V. et al 2006 Plasma Phys. Control. Fusion 48 839
[31] Bonnin X. et al 2016 Plasma Fusion Res. 11 1403102–1403102
[32] https://open.adas.ac.uk/
[33] Gao F. et al 2020 Nucl. Fusion 60 066022
[34] Futatani S. et al 2014 Nucl. Fusion 54 073008
[35] Palade D I 2023 *Nucl. Fusion* **63** 046007
[36] Jia G. *et al* 2022 *Nucl. Fusion* **62** 056005
[37] Sang C. *et al* 2016 *Nucl. Fusion* **56** 106018
[38] Canik J.M. *et al* 2018 *IEEE Trans. Plasma Sci.* **46** 1081–5
[39] Rozhansky V. *et al* 2003 *J. Nucl. Mater.*
[40] Bonnin X. *et al* 2005 *J. Nucl. Mater.* **337–339** 301–4
[41] Hoshino K. *et al* 2006 *Contrib. Plasma Phys.* **46** 591–6
[42] Liu J B. *et al* 2016 *Nucl. Fusion* **56** 066006
[43] Rozhansky V. *et al* 2013 *J. Nucl. Mater.* **438** S297–302
[44] Wang F. *et al* 2022 *Nucl. Fusion* **62** 056021
[45] Paradela Pérez.I. *et al* 2019 *Nucl. Mater. Energy* **19** 531–6
[46] Ma X. *et al* 2021 *Nucl. Fusion* **61** 054002
[47] Xu J.C. *et al* 2021 *Nucl. Fusion* **61** 096004
[48] Wang D. *et al* 2011 *Phys. Plasmas* **18** 032505
[49] Liu S C. *et al* 2014 *Phys. Plasmas* **21** 122514
[50] Du H. *et al* 2016 *Fusion Eng. Des.* **109–111** 1005–10
[51] Wang R. *et al* 2022 *Phys. Plasmas* **29** 112502
[52] Pan O. *et al* 2020 *Plasma Phys. Control. Fusion* **62** 045005
[53] Stangeby P.C. 2000 (Bristol ; Philadelphia: Institute of Physics Pub)
[54] Verhaegh K. *et al* 2019 *Nucl. Fusion* **59** 126038
[55] Tokar M.Z. 2008 *Fusion Sci. Technol.* **53** 243–50
[56] Chen Y. *et al* 2014 *Plasma Phys. Control. Fusion* **56** 105006
[57] Groth M. *et al* 2002 *Nucl. Fusion* **42** 591–600
[58] Chrobak C.P. S *et al* 2018 *Nucl. Fusion* **58** 106019
[59] Meng L.Y. *et al* 2022 *Nucl. Fusion* **62** 086027
[60] Dai S.Y. *et al* 2022 *Nucl. Fusion* **62** 036019
[61] Wang F. *et al* 2023 *Plasma Sci. Technol.* **25** 115102

[62] Pütterich T. *et al* 2019 *Nucl. Fusion* **59** 056013